This is the peer-reviewed, final accepted version for American Mineralogist, published by the Mineralogical Society of America.
The published version is subject to change. Cite as Authors (Year) Title. American Mineralogist, in press.
DOI: https://doi.org/10.2138/am-2021-7605. http://www.minsocam.org/

Revision 2

Word count: 5587

Electrical conductivity of diaspore, δ-AlOOH and ε-FeOOH

Ran Wang*, Takashi Yoshino

Institute for Planetary Materials, Okayama University, Misasa, Tottori 682-0193, Japan

ABSTRACT

Electrical conductivities of diaspore (α-AlOOH), δ-AlOOH and ε-FeOOH were measured by impedance spectroscopy with a frequency range from 10^{-1} to 10^{6} Hz at pressures up to 15, 20 and 20 GPa and temperatures up to 1200, 1200 and 1000 K, respectively, well below the dehydration temperatures of these phases at the relevant pressures. For diaspore, the relationship between electrical conductivity and reciprocal temperature can be well fitted by the Arrhenius formula: $\sigma = \sigma_0 \exp\left[\frac{-(\Delta E + P\Delta V)}{kT}\right]$, where σ_0 is the pre-exponential factor, ΔE is activation energy, and ΔV is activation volume of 56.0 ± 1.2 S/m, 0.55 ± 0.02 eV and 1.68 ± 0.12 cm^3/mol, respectively. The electrical conductivity of diaspore decreases with increasing pressure ranging from 8 to 12 GPa by a half order of magnitude, whereas the conductivity becomes almost constant in a pressure range above 12 GPa. δ-AlOOH and ε-FeOOH show one and two orders of magnitude higher electrical conductivity than diaspore. Electrical conductivities of δ-AlOOH and ε-FeOOH, which have isostructural $CaCl_2$-type hydroxide structure, show the nearly identical activation enthalpies (0.38 ± 0.01 eV, 0.33 ± 0.05 eV), which are relatively lower than that of diaspore. The dominant conduction

mechanism of AlOOH phases can be regarded as proton conduction. The conductivity difference between diaspore and δ-AlOOH attributes to result in the different O_1H bond lengths of each phase. The reduction of O_1H bond length with increasing pressure could enhance the proton migration by reducing the potential barrier, thereby raises the electrical conductivity. Small polaron conduction may contribute to the conductivity of ε-FeOOH to generate higher conductivity than δ-AlOOH. Furthermore, hydrogen bond symmetrization will also play an important role on the conductivity discrepancy of these hydrous minerals with $CaCl_2$-type hydroxide structure. For the subducted sedimentary rocks, polymorphs of AlOOH and FeOOH are representative hydrous phases. Al-rich sediments shows conductivity reduction with increasing depth until phase transformation occurs, because diaspore represents negative pressure dependence of conductivity. After transformation to δ-AlOOH, the conductivity will jump up around 18 GPa. If ε-FeOOH is stable above 5 GPa in the highly iron-rich lithology such as banded iron formation (BIF), high conductivity zone with positive pressure dependence could be observed to the deep lower mantle.

Keywords: Electrical conductivity, diaspore, δ-AlOOH, ε-FeOOH, hydrogen bond

INTRODUCTION

Water has significant influence on dynamics and deep element cycle processes in the Earth's interior such as slab subduction, mantle convection and volcanisms. Recently, many groups focused on studies on the water content of the Earth's interior in terms of electrical

conductivity (e.g., Wang et al., 2006; Romano et al., 2009; Yoshino and Katsura, 2013) and potential paths to carry multiform water (hydrogen, hydroxyl and H_2O) into transition zone and even lower mantle (e.g., Ohtani et al., 2001; 2018). Many studies have proposed that hydrous minerals such as dense hydrous Mg silicates (DHMS) are potential water carriers to transition zone and lower mantle (Frost et al. 1998; Ono, 1998; Schmidt et al., 1998; Nishi et al., 2014; Pamato et al., 2015). Indeed, hydrous minerals and nominally anhydrous minerals containing significant amount of water were found in diamond inclusion from the kimberlite suite (Wirth et al., 2007; Pearson et al., 2014), suggesting that at least some portions in the Earth's mantle store the water. Meanwhile, recent experimental studies have shown that high pressure polymorphs of AlOOH and FeOOH are stable in the lower mantle along the normal geotherm (Sano et al., 2008; Nishi et al., 2017; Duan et al., 2018; Hu et al., 2016, 2017).

Electrical conductivity has been used as an effective tool to determine water contents in the Earth's mantle because the conductivity has been believed to be quite sensitive to water content in nominally anhydrous minerals (e.g., Karato, 1990; Huang et al., 2005; Wang et al., 2006; Yoshino et al., 2006; 2008). Electrical conductivity of hydrous minerals would be useful to constrain water distribution in the Earth's interior, especially the subduction zone. For this purpose, many researchers have measured electrical conductivity of hydrous minerals such as serpentine, lawsonite, mica, DHMS (Guo et al., 2011; Guo and Yoshino, 2013; Manthilake et al., 2015; Pommier et al., 2019; Chen et al., 2019). These studies have

shown different pressure dependence due to the difference of their crystal structures. For example, brucite shows positive pressure dependence (Guo and Yoshino, 2014), induced by a shortening of O···O distance in hydrogen interlayer between (MgO_6) octahedron, whereas phengite shows negative pressure dependence (Chen et al., 2017) probably because of absence of face to face hydrogen layer. To understand the pressure effect on electrical conductivity of hydrous minerals, more studies on hydrous minerals with simple structure are more effective. Electrical conductivities of AlOOH and FeOOH, which are hydrous phases with the simplest chemical formulae, have not been reported yet, although these phases are main hydrous phases in subducting sedimentary rocks (Xu et al., 2019; Yoshino et al., 2019).

In this study, we measured the electrical conductivity of diaspore (α-AlOOH), δ-AlOOH and ε-FeOOH well below their dehydration temperatures (1273K, 1473K and 1073k) to avoid contribution of dehydrated water to the measured conductivity (Suzuki et al., 2000; Ohtani et al., 2001). Both δ-AlOOH and ε-FeOOH have the identical crystal structure that are characterized by hydrogen interlayer between (AlO_6) or (FeO_6) octahedron, corresponding to the $CaCl_2$-type InOOH crystal structure (Kudoh et al., 2004; Otte et al., 2009; Tsuchiya and Tsuchiya, 2009; 2011; Kagi et al., 2010; Sano-Furukawa et al., 2018). On the other hand, diaspore has different crystal structure from δ-AlOOH and ε-FeOOH (Winkler et al., 2001; Friedrich et al., 2007). Therefore, electrical conductivity measurements of diaspore, δ-AlOOH and ε-FeOOH are useful to understand the influence

of crystal structure especially the change of O_1-H$\cdots O_2$ bond length during compression on the electrical conductivity of hydrous minerals.

EXPERIMENTAL METHODS

Starting material

The starting material for FeOOH was reagent-grade goethite (α-FeOOH) powder from Alfa Aeser. The starting material for AlOOH was powder prepared from a single crystal of natural diaspore from Turkey, which contains considerable amounts of Fe_2O_3 (0.82 ± 0.08 wt%) (Yoshino et al., 2019). The sintered aggregates were used for the conductivity measurement to reduce porosity of the sample, and synthesized in a Kawai-type multi-anvil apparatus installed in the Institute for Planetary Materials, Okayama University. The cell assemblies for synthesis experiments are composed of a Cr_2O_3-doped MgO octahedral pressure medium, ZrO_2 thermal insulator, graphite or $LaCrO_3$ heater, MgO spacer and the powdered AlOOH and FeOOH samples were sealed in Pt and Au capsules, respectively. The octahedron edge lengths of the pressure medium and truncations edge length of anvils for synthesis experiments are summarized in Table 1. Diaspore aggregate was sintered at 8 GPa and 973 K. Starting samples of δ-AlOOH and ε-FeOOH aggregates were synthesized at 19 GPa, 1273 K and 9 GPa, 700 K, respectively, based on the sintering procedure by Suzuki et al. (2000) and Suzuki (2016). The phases of run products (Fig. 1 and Table 1) were identified by X-ray diffraction patterns using microfocus X-ray diffraction in reflection geometry (collimator with 0.1 mm diameter).

No change was observed in the x-ray diffraction patterns before and after the experiment. If dehydration occurred during the measurements, some peaks of other phases such as corundum (Al_2O_3) and hematite (Fe_2O_3) could be observed in the XRD patterns. The XRD patterns infer that there is no obvious dehydration occurring in the samples. The recovered samples were observed by field emission scanning electron microscope. Fig. 2 shows the backscattered electron images on the polished section of the recovered samples. No phases such as corundum and hematite produced by dehydration reaction was found in all the recovered samples. The grain sizes of these recovered samples are shown in Table 2 (Kong et al., 2005).

Electrical conductivity measurement

The cell design for electrical conductivity measurements in a Kawai-type cell was developed by Yoshino (2010). The load-pressure relation for this cell assembly determined by Yoshino et al. (2017) was used for the pressure estimation. Electrical conductivity measurements were performed using a complex impedance analyzer (Solartron 1260) with a frequency range from 10^{-1} to 10^{6} Hz. One wire from each thermocouple were connected to a Solartron 1296 interface for measuring the electrical conductivity of the sample. Alternating current with amplitude of 1 V was applied to the measurement circuit. The impedance spectra show semi-circular shape and its intersection on horizontal axis represents the real resistance of the sample. Resistance (R)-capacitance (C) parallel circuit was used to fit the impedance spectrum obtained from the electric circuit. The sample

conductivity was calculated from the following equation: $\sigma = \frac{1}{\rho} = \frac{L}{RS}$, where ρ is electrical resistivity, L is sample length, and S is cross sectional area of the sample. The details of experimental conditions are summarized in Table 3.

RESULTS

All the conductivity measurements were performed below the dehydration temperature (1273K, 1473K and 1073k) of each phase (Ohtani et al., 2001; Yoshino et al., 2019). Fig. 3 shows examples of impedance spectra of diaspore, δ-AlOOH, and ε-FeOOH at 8, 20 and 8 GPa, respectively, as a function of temperature. Impedance spectra of diaspore show semi-circular shape in complex impedance plane. However, for δ-AlOOH and ε-FeOOH with high electrical conductivity, only a portion of semi-circular shape appears in the same frequency range applied for all the experiments. The small tails of impedance spectra indicate the interaction between samples and electrodes at lower frequencies.

Fig. 4 shows the electrical conductivity of the diaspore, δ-AlOOH and ε-FeOOH during cooling at various pressures as a function of the reciprocal temperature. In any phase, electrical conductivity linearly increases with increasing temperature. Arrhenius formula was used to fit the relationship between electrical conductivity and reciprocal temperature:

$$\sigma = \sigma_0 \exp\left[-\frac{\Delta E + P\Delta V}{\mathrm{k}T}\right], \qquad \text{Eq. (1)}$$

where σ_0, ΔE, P, ΔV, k, and T are pre-exponential factor, activation energy, pressure, activation volume, Planck constant and absolute temperature, respectively. For each experiment, the ΔE and ΔV were determined from the global fitting using all the data

obtained at different *P* and *T*.

The diaspore shows negative pressure dependence on electrical conductivity ranging from 8 to 12 GPa. However, the conductivity becomes constant in a pressure range between 12 and 15 GPa. The electrical conductivity of δ-AlOOH shows one and two orders of magnitude higher than diaspore and much smaller ΔE. Although the electrical conductivity of ε-FeOOH is higher than δ-AlOOH, the ΔE for conductivity of ε-FeOOH (0.38 ± 0.01 eV) is similar to that of δ-AlOOH (0.33 ± 0.05 eV). ε-FeOOH shows positive pressure dependence on electrical conductivity in an investigated pressure range (8 to 20 GPa). Fig. 5 shows the fitting results of diaspore conductivity using data ranging from 8 to 12 GPa. The σ_0, ΔE and ΔV are found to be 56.0 ± 1.2 S/m, 0.55 ± 0.02 eV and 1.68 ± 0.12 cm^3/mol, respectively.

DISCUSSION

Conduction mechanisms of diaspore, δ-AlOOH and ε-FeOOH

In hydrous minerals, proton conduction has been considered to be the dominant conduction mechanism (Freund et al., 1981; Guo and Yoshino, 2014; Chen et al., 2018). While increasing temperature, proton could be produced through the thermally activation process:

$$OH^- + OH^- = HOH + O^{2-}, \qquad \text{Eq. (2)}$$

where HOH is the hydroxyl with an extra proton on the lattice site and O^{2-} represents a defect proton (chemically O^{2-}) (Martens and Freund, 1976; Guo and Yoshino, 2014).

Therefore, protons would be able to migrate along the adjacent hydroxyls through two paths:

$$HOH + OH^- = OH^- + HOH, \quad \text{Eq. (3)}$$

or

$$O^{2-} + OH^- = OH^- + O^{2-} \quad \text{Eq. (4)}$$

In Eq. (2), the protons are thermally activated during heating which is called intrinsic mechanism. In Eq. (3 and 4), the defects related to proton mobility are also generated by the existence of chemical impurities, and protons can migrate due to compensation of charge balance.

This study demonstrates three significant features among diaspore, ε-FeOOH and δ-AlOOH: (1) ε-FeOOH and δ-AlOOH have one and two orders of magnitude higher conductivity than diaspore; (2) ε-FeOOH has much higher conductivity than δ-AlOOH. (3) Diaspore shows negative pressure dependence while ε-FeOOH shows positive pressure dependence.

(1) ε-FeOOH and δ-AlOOH have isostructural $CaCl_2$-type hydroxide structure which is different from diaspore. The space group of diaspore is Pbnm while both ε-FeOOH and δ-AlOOH are $P2_1nm$. Different crystal structure leads to variable compressible behaviors during compression. If proton conduction is the dominant conduction mechanism in these phases, the proton exchange in those minerals may occur by reaction Eq. (3). Therefore, the length of O_1H and $H\cdots O_2$ bonds becomes a significant factor on their conductive

behaviors. During compression, the O_1H bond will elongate and become weaker which may produce the free proton and combine with another proton defect (O^{2-}). δ-AlOOH and ε-FeOOH have shorter $H\cdots O_2$ bonds and longer O_1H bonds which can account for the relatively higher conductivity than diaspore (Friedrich et al., 2007; Gleason et al., 2013; Cedillo et al., 2016).

(2) Although ε-FeOOH and δ-AlOOH have the same crystal structure, there are some differences between them. One possible explanation for higher conductivity of ε-FeOOH is that ε-FeOOH has shorter $H\cdots O_2$ bond than δ-AlOOH at 20 GPa (Cedillo et al., 2016; Thompson et al., 2017). Besides, the symmetry of O_1-$H\cdots O_2$ bond changes with increasing pressure. Hydrogen bond symmetrization of δ-AlOOH occurs at 15~18 GPa (Cortona, 2017; Sano-Furukawa et al., 2018), whereas hydrogen bond in ε-FeOOH is predicted to symmetrize around 40 GPa (Gleason et al., 2013). In this study, the conductivity of δ-AlOOH was measured at 20 GPa, which is higher than the pressure at which symmetrization of the O_1-$H\cdots O_2$ bond occurs. After reaching this pressure, the O_1-$H\cdots O_2$ bond becomes covalent and it will be difficult for proton to migrate through lattice sites, suggesting that the pressure-induced effect become negligible. Since the experimental pressures for ε-FeOOH are much lower than the hydrogen symmetrization pressure (40 GPa), the conductivity of ε-FeOOH can increase effectively by compression in the investigated pressure range. Alternatively, if the ε-FeOOH contains significant amount of Fe^{2+} through the substitution: $Fe^{3+} = Fe^{2+} + H^+$, small polaron conduction would yield

enormous contributions to the conductivity. A study on electrical conductivity and hydrogen diffusivity of brucite suggests that all hydrogen would not contribute to the electrical conduction in hydrous minerals (Guo and Yoshino, 2014). Compared with δ-AlOOH, ε-FeOOH would considerably enhance electric conductivity by activating a greater numbers of protons by the reaction of $Fe^{3+} = Fe^{2+} + H^{+}$.

(3) For diaspore, the length of O_1H bond slightly increases with increasing pressure (Friedrich et al., 2007). Therefore, pressure-induced effects are not effective for diaspore unlike δ-AlOOH. As the O_1-H···O_2 bond becomes more symmetric, protons become more difficult to migrate due to the enhanced hydrogen bond strength which cause the negative pressure dependence on the conductivity. In contrast, δ-AlOOH and ε-FeOOH show obviously larger change on the length of O_1H bond during compression (Gleason et al., 2013; Cedillo et al., 2016). The O_1H bond strength becomes weaker and then protons are more likely to migrate through lattice sites. As a result, the conductivity of ε-FeOOH can be enhanced by pressure. As described before, hydrogen bond symmetrization occurs in δ-AlOOH and ε-FeOOH at 15~18 and 40 GPa, respectively, which will weaken the O_1H bond and strengthen the H···O_2 bond to yield higher conductivity. However, hydrogen bond in diaspore never symmetrizes (Friedrich et al., 2007; Tsuchiya and Tsuchiya, 2011). This may be caused by the difference of O_1-H···O_2 bond angle in the crystal structure of these phases. The angle of O_1-H···O_2 bond in δ-AlOOH is almost 180° while that in diaspore is bent (160°) (Cedillo et al., 2016; Friedrich et al., 2007). The O_1-H···O_2 bond angle of

diaspore should show minor variations during compression. The O_1-H$\cdots O_2$ bond symmetrization in ε-FeOOH will cause the increment of the length of OH bond and shortening of hydrogen bond which will enhance the migration of the hydrogen (proton). This could be the other cause of the opposite pressure dependence on conductivity of diaspore and ε-FeOOH.

Comparison with other hydrous minerals

Many studies were conducted on the measurements of electrical conductivities of hydrous minerals in a wide range of pressure. Guo and Yoshino (2014) reported that the electrical conductivity of brucite has positive pressure dependence. Proton conduction was suggested to be the dominant conduction mechanism and Eq. (4) was the most favorable reaction for the proton exchange. The explanation for the positive pressure dependence on conductivity is that $O_1\cdots O_2$ distance deceases with increasing pressure which will lead to the reduction of the potential barrier between proton sites in adjacent OH^- groups. This shows an agreement with the ε-FeOOH result. With increasing pressure, the O_1H bond becomes weaker and protons are easier to escape from the attractive force of O_1 which will help to increase the conductivity. Meanwhile, the conductivities of samples under different pressures do not converge at high temperatures, suggesting that the activation enthalpy does not change dramatically with increasing pressure which is consistent with the result of ε-FeOOH.

Pommier et al. (2019) showed that the electrical conductivity of natural lawsonite has

positive pressure dependence between 5 and 9 GPa. All the lattice parameters (*a*, *b*, *c* axis) decrease with increasing pressure (Comodi and Zanazzi, 1996) which may enhance the conductivity of lawsonite. Molecular H_2O is also contained in the crystal structure of lawsonite which may play an important role on the conductivity during compression because the dominant conduction mechanism is presented as proton conduction. Chen et al. (2018) reported a negative pressure dependence on conductivity of phengite. The negative pressure dependence was explained by the non-existence of face to face hydrogen layer and interactions between neighboring hydroxyls in phengite. Pressure cannot enhance the conductivity by markedly elongating the O_1H bond as well as diaspore. Besides, the conductivities of phengite at different pressures converge together at high temperature as well as the behavior of diaspore.

IMPLICATIONS

According to the crystal structure of hydrous minerals, we can predict trends of the conductivity-depth relation for various lithologies including hydrous minerals in subduction zone as shown in Fig. 6. Lawsonite and phengite are representative hydrous phases of the subducted altered oceanic crust. Lawsonite has larger conductivity than phengite at some *P-T* condition, suggesting that lawsonite will contribute to the conductivity of the subducted MORB. If lawsonite is interconnected phase, it may indicate positive pressure dependence with depths until dehydration occurs at around 10 GPa for the cold slab (e.g., Schmidt and Poli, 1998; Okamoto and Maruyama, 1999). Although

phengite can survive a bit higher pressure, this phase will not contribute to the conductivity of the hydrous MORB because of its negative pressure dependence. For the hydrous peridotite, one can notice that DHMS phases transform from phase A to superhydrous phase B (or phase E) and phase D with increasing pressure (Ohtani et al., 2001). The resulting conductivity variation with depth should have positive dependence. For the subducted sediments with average composition of continental crust, phengite is considered to be a dominant hydrous phase below 8 GPa. For more Al-rich sediments, diaspore could be dominant hydrous phases. Thus, electrical conductivity of the sedimentary rocks would generally decrease with depth. Goethite is only dominant in the highly iron-rich lithology such as banded iron formation. The stability field of goethite is limited at pressures below 5 GPa (Yoshino et al., 2019). In this region, the conductivity of the subducted sedimentary rocks would decrease with increasing pressure. ε-FeOOH could be stabilized if the rehydration of subducted Fe-rich sediments occurs at pressures higher than 5 GPa. On account of the extremely higher conductivity of ε-FeOOH, highly conductive zone with positive pressure dependence should appear in the descending slab.

Fig. 7 shows the comparison of conductivity-depth profiles calculated from diaspore, δ-AlOOH and ε-FeOOH along cold (the North Philippine Sea) and hot slab surface geotherms (the North Cascadia) and magnetotelluric observations from the above subduction zones. The conductivity-depth profiles of diaspore were calculated through the Arrhenius formula: $\sigma = \sigma_0 \exp\left[\frac{-(\Delta E + P\Delta V)}{kT}\right]$ by inputting the σ_0 (56.0 ± 1.2 S/m), ΔE

279 (0.55 ± 0.02 eV), and ΔV (1.68 ± 0.12 cm^3/mol). Considering the stability fields of diaspore,
280 δ-AlOOH and ε-FeOOH (Yoshino et al., 2019), we plot the conductivity-depth profile of
281 these phases. Diaspore can exist below 2.3 and 1.8 GPa for the North Philippine Sea and
282 the North Cascadia slab surface geotherms (Syracuse et al., 2010), and shows lower
283 conductivity compared with conductivity-depth profiles of both slabs (Meqbel et al., 2014).
284 For ε-FeOOH, we used σ_0 (512.9 ± 1.8 S/m), ΔE (0.46 ± 0.03 eV), and ΔV (-1.52 ± 0.13
285 cm^3/mol) for the calculation of conductivity-depth profile. If the rehydration of ε-FeOOH
286 occurred, ε-FeOOH would appear above 15 GPa along the extrapolation of the North
287 Philippine Sea slab surface geotherm, and represents distinctly higher conductivity values.
288 The comparison between this study and the geophysical observations indicate that diaspore
289 and ε-FeOOH cannot account for the electrical anomalies in the upper mantle because of
290 the decompositions of these two phases and the lower conductivities compared to the
291 conductivity profiles of both hot and cold slabs. Thus, the volume fraction of these phases
292 is negligibly small in the present subduction zones. In contrast, the absolute conductivity
293 values of δ-AlOOH are comparable to the extrapolation of conductivity-depth profiles
294 obtained from subduction zones.

295 **ACKNOWLEDGEMENTS**

296 We appreciate it for the constructive suggestions or comments from B. Zhang, C. Wang,
297 M. Kanzaki, D. Yamazaki, N. Tsujino, E. Ito, A. Yoneda, H. Kagi and J. Tsuchiya. This
298 work was supported by the Ministry of Education, Culture, Sports, Science, and

Technology of the Japanese Government, Grant Numbers, 15H05827 and 17H01155 to T.Y.

REFERENCES

Cedillo, A., Torrent, M. and Cortona, P. (2016) Stability of the different AlOOH phases under pressure. Journal of Physics: Condensed Matter, 28, 185401.

Chen, S., Guo, X., Yoshino, T., Jin, Z., and Li, P. (2018) Dehydration of phengite inferred by electrical conductivity measurements: Implication for the high conductivity anomalies relevant to the subduction zones. Geology, 46, 11–14.

Comodi, P., Zanazzi, P. (1996) Effects of temperature and pressure on the structure of lawsonite. American Mineralogist, 81, 833-841.

Cortona, P. (2017) Hydrogen bond symmetrization and elastic constants under pressure of δ-AlOOH. Journal of Physics: Condensed Matter, 29, 325505.

Duan, Y., Sun, N., Wang, S., Li, X., Guo, X., Ni, H., Prakapenka, V.B., Mao, Z. (2018) Phase stability and thermal equation of state of δ-AlOOH: Implication for water transportation to the Deep Lower Mantle. Earth and Planetary Science Letters. 494, 92–98.

Freund, F., Wengeler, H., Martens, R. (1982) A deuterium-hydrogen fractionation mechanism in magnesium oxide. Geochimica et Cosmochimica Acta, 46, 1821-1829.

Friedrich, A., Haussühl, E., Boehler, R., Morgenroth, W., Juarez-Arellano, E.A., and Winkler, B. (2007) Single-crystal structure refinement of diaspore at 50 GPa. American Mineralogist, 92, 1640–1644.

Frost, D., Fei, Y. (1998) The stability of phase D at high pressure and temperature, Journal of Geophysical Research. 103, 7463–7474.

Gleason, A., Quiroga, C., Suzuki, A., Pentcheva, R., Mao, W. (2013) Symmetrization driven spin transition in ε-FeOOH at high pressure. Earth and Planetary Science Letters, 379, 49–55.

Guo, X., Yoshino, T., Katayama, I. (2011) Electrical conductivity anisotropy of deformed talc rocks and serpentinites at 3 GPa. Physics of the Earth and Planetary Interiors, 188, 69–81.

Guo, X., Yoshino, T. (2013) Electrical conductivity of dense hydrous magnesium silicates with implication for conductivity in the stagnant slab. Earth and Planetary Science Letters, 369–370, 239–247.

Guo, X., Yoshino, T. (2014) Pressure-induced enhancement of proton conduction in brucite. Geophysical Research Letters, 41, 813–819.

Hu, Q., Kim, D.Y., Yang, W., Yang, L., Meng, Y., Zhang, L., and Mao, H.K. (2016) FeO2 and FeOOH under deep lower-mantle conditions and Earth's oxygen-hydrogen cycles. Nature, 534(7606):241–244.

Hu, Q., Kim, D.Y., Liu, J., Meng, Y., Yang, L., Zhang, D., Mao, W.L., and Mao, H.K. (2017) Dehydrogenation of goethite in Earth's deep lower mantle. Proceedings of the National Academy of Sciences. 114, 1498-1501.

Huang, X., Xu, Y., Karato, S. (2005) Water content in the transition zone from electrical conductivity of wadsleyite and ringwoodite. Nature, 434, 746–49.

Kagi, H., Ushijima, D., Sano-Furukawa, A., Komatsu, K., Iizuka, R., Nagai, T. and Nakano, S. (2010) Infrared absorption spectra of δ-AlOOH and its deuteride at high pressure and implication to pressure response of the hydrogen bonds. Journal of Physics: Conference Series, 215, 012052.

Karato, S. (1990) The role of hydrogen in the electrical conductivity of the upper mantle. Nature, 347, 272–273.

Kong, M., Bhattacharya, R. N., James, C. and Basu, A. (2005) A statistical approach to estimate the 3D size distribution of spheres from 2D size distributions. Geological Society of America Bulletin, 117, 244-249.

Kudoh, Y., Kuribayashi, T., Suzuki, A., Ohtani, E., Kamada, T. (2004) Space group and hydrogen sites of d-AlOOH and implications for a hypothetical high-pressure form of $Mg(OH)_2$. Physics and Chemistry of Minerals, 31, 360–364.

Manthilake, G., Mookherjee, M., Casanova, N., Andrault, D. (2015) Electrical conductivity of lawsonite and dehydrating fluids at high pressures and temperatures. Geophysical Research Letters, 42, 7398–7405.Martens, R., Freund, F. (1976) The potential energy curve of the proton and dissociation energy of the OH ion in $Mg(OH)_2$. Physica Status Solidi A, 37, 97–104.

Meqbel, N.M., Egbert, G.D., Wannamaker, P.E., Kelbert, A., and Schultz, A. (2014) Deep electrical resistivity structure of the northwestern US derived from 3-D inversion of USArray magnetotelluric data. Earth and Planetary Science Letters, 402, 290–304.

Nishi, M., Irifune, T., Tsuchiya, J., Tange, Y., Nishihara, Y., Fujino, K. and Higo, Y. (2014) Stability of hydrous silicate at high pressures and water transport to the deep lower mantle. Nature Geoscience, 7, 224–227.

Nishi, M., Kuwayama, Y., Tsuchiya, J.& Tsuchiya, T. (2017) The pyrite-type high-pressure form of FeOOH. Nature, 547, 205-208.

359 Ohtani, E., Mizobata, H., Yurimoto, H. (2000) Stability of dense hydrous magnesium silicate phases in
360 the systems Mg_2SiO_4-H_2O and $MgSiO_3$-H_2O at pressures up to 27 GPa. Physics and Chemistry of
361 Minerals, 27, 533–544.
362 Ohtani, E., Litasov, K., Suzuki, A., and Kondo, T. (2001) Stability field of new hydrous phase, δ-AlOOH,
363 with implications for water transport into the deep mantle. Geophysical Research Letters, 28, 3991–
364 3993.
365 Ohtani, E., Yuan, L., Ohira, I., Shatskiy, A., Litasov, K. (2018) Fate of water transported into the deep
366 mantle by slab subduction. Journal of Asian Earth Sciences, 167, 2-10.
367 Okamoto, K., Maruyama, S. (1999) The high-pressure synthesis of lawsonite in the MORB+H_2O system.
368 American Mineralogist, 84, 362–373.
369 Ono, S. (1998) Stability limits of hydrous minerals in sediment and mid-ocean ridge basalt compositions:
370 implications for water transport in subduction zones. Journal of Geophysical Research. 103,
371 18253–18267.
372 Otte, K., Pentcheva, R., Schmahl, W., and Rustad, J. (2009) Pressure-induced structural and electronic
373 transitions in FeOOH from first principles. Physical Review B, 80, 205116.
374 Pamato, M., Myhill, R., Ballaran, T., Frost, D., Heidelbach, F., Miyajima, N. (2015) Lower-mantle water
375 reservoir implied by the extreme stability of a hydrous aluminosilicate. Nature Geoscience, 8, 75–
376 79.
377 Pawley, A. (1994) The pressure and temperature stability limits of lawsonite: implications for HzO
378 recycling in subduction zones. Contributions to Mineralogy and Petrology, 118, 99–108.

379 Pearson, D.G., Brenker, F.E., Nestola, F., McNeill, J., Nasdala, L., Hutchison, M.T., Matveev, S., Mather,
380 K., Silversmit, G., Schmitz, S., Vekemans, B., Vincze, L. (2014) Hydrous mantle transition zone
381 indicated by ringwoodite included within diamond. Nature, 507, 221–224.
382 Pommier, A., Williams, Q., Evans, R., Pal, I., and Zhang, Z. (2019) Electrical Investigation of Natural
383 Lawsonite and Application to Subduction Contexts. Journal of Geophysical Research: Solid Earth,
384 124, 1430–1442.
385 Romano, C., Poe, B., Tyburczy, J., Nestola, F. (2009) Electrical conductivity of hydrous wadsleyite.
386 European Journal of Mineralogy, 21, 615–622.
387 RRUFF. XRD pattern of diaspore. https://rruff.info/Diaspore/R060287.
388 Sano, A., Ohtani, E., Kondo, T., Hirao, N., Sakai, T., Sata, N., Ohishi, y., and Kikegawa, T. (2008)
389 Aluminous hydrous mineral δ-AlOOH as a carrier of hydrogen into the core-mantle boundary.
390 Geophysical Research Letters, 35, L03303.
391 Sano-Furukawa, A., Hattori, T., Komatsu, K., Kagi, H., Nagai, T., Molaison, J., Santos, A. & Tulk, C.
392 (2018) Direct observation of symmetrization of hydrogen bond in δ-AlOOH under mantle
393 conditions using neutron diffraction. Scientific Reports, 8, 15520.
394 Schmidt, M.W., Poli, S.. (1998) Experimentally based water budgets for dehydrating slabs and
395 consequences for arc magma generation. Earth and Planetary Science Letters. 163, 361–379.
396 Suzuki, A., Ohtani, E., and Kamada, T. (2000) A new hydrous phase δ-AlOOH synthesized at 21 GPa
397 and 1000 °C. Physics and Chemistry of Minerals, 27, 689–693.
398 Suzuki, A. (2016) Pressure–volume–temperature equation of state of ε–FeOOH to 11 GPa and 700 K.

399 Journal of Mineralogical and Petrological Sciences, 111, 420–424.

400 Syracuse, E.M., van Keken, P.E., and Abers, G.A. (2010) The global range of sub- duction zone thermal
401 models. Physics of the Earth and Planetary Interiors, 183, 73–90.

402 Tada, N., Baba, K., and Utada, H. (2014) Three-dimensional inversion of seafloor magnetotelluric data
403 collected in the Philippine Sea and the western margin of the northwest Pacific Ocean.
404 Geochemistry, Geophysics, Geosystems, 15, 2895–2917.

405 Thompson, E., Campbell, A., Tsuchiya, J. (2017) Elasticity of ε-FeOOH: Seismic implications for
406 Earth's lower mantle. Journal of Geophysical Research: Solid Earth, 122, 5038–5047.

407 Tsuchiya, J. & Tsuchiya, T. (2009) Elastic properties of δ-AlOOH under pressure: First principles
408 investigation. Physics of the Earth and Planetary Interiors, 174, 122–127.

409 Tsuchiya, J. & Tsuchiya, T. (2011) First-principles prediction of a high-pressure hydrous phase of
410 AlOOH. Physical Review B, 83, 054115.

411 Wang, D., Mookherjee, M., Xu, Y., Karato, S. (2006) The effect of water on electrical conductivity of
412 olivine. Nature, 443, 977–79.

413 Winkler, B., Hytha, M., Pickard, C., Milman, V., Warren, M. and Segall, M. (2001) Theoretical
414 investigation of bonding in diaspore. European Journal of Mineralogy. 13, 343–349.

415 Wirth, R., Vollmer, C., Brenker, F., Matsyuk, S., Kaminsky, F. (2007) Inclusions of nanocrystalline
416 hydrous aluminium silicate “Phase Egg” in superdeep diamonds from Juina (Mato Grosso State,
417 Brazil). Earth and Planetary Science Letters, 259, 384–399.

418 Xu, C., Nishi, M., Inoue, T. (2019) Solubility behavior of δ-AlOOH and ε-FeOOH at high pressures.

American Mineralogist, 104, 1416–1420.

Yoshino, T., Matsuzaki, T., Yamashita, S., Katsura, T. (2006) Hydrous olivine unable to account for conductivity anomaly at the top of the asthenosphere. Nature, 443, 973–976.

Yoshino, T., Manthilake, G., Matsuzaki, T., Katsura T. (2008) Dry mantle transition zone inferred from the conductivity of wadsleyite and ringwoodite. Nature, 451, 326–329.

Yoshino, T., (2010) Laboratory electrical conductivity measurement of mantle minerals. Surveys in Geophysics, 31, 163-206.

Yoshino, T., Katsura, T. (2013) Electrical Conductivity of Mantle Minerals: Role of Water in Conductivity Anomalies. Annual Review of Earth and Planetary Sciences, 41, 605–28.

Yoshino, T., Zhang, B., Rhymer, B., Zhao, C., and Fei, H. (2017) Pressure dependence of electrical conductivity in forsterite. Journal of Geophysical Research: Solid Earth, 122, 158–171.

Yoshino, T., Baker, E., Duffey, K. (2019) Fate of water in subducted hydrous sediments deduced from stability fields of FeOOH and AlOOH up to 20 GPa. Physics of the Earth and Planetary Interiors, 294, 106295.

433 **Fig. 1.** XRD pattern of samples before and after measurements. **(a)** XRD pattern of
434 diaspore before and after conductivity measurements compared with that of RRUFF
435 database. **(b)** XRD patter of δ-AlOOH before and after conductivity measurements
436 compared with Suzuki et al. (2000). **(c)** XRD patter of ε-FeOOH before and after
437 conductivity measurements compared with Pernet (1975).
438
439 **Fig. 2.** Backscattered electron images of recovered products after electrical conductivity
440 measurements under composition mode. **(a)** Diaspore under 8, 10, 12 and 15 GPa; **(b)** ε-
441 FeOOH under 8 and 10 GPa; **(c)** δ-AlOOH under 20 GPa; **(d)** ε-FeOOH under 20 GPa.
442 Note that no presence of phase associated with dehydration.
443
444 **Fig. 3.** Impedance spectra of electrical conductivity measurement. **(a)** Impedance
445 spectrum of diaspore at 8 GPa. **(b)** Impedance spectrum of δ-AlOOH at 20 GPa. **(c)**
446 Impedance spectrum of ε-FeOOH at 8 GPa. Z' and Z'' are real and imaginary parts of the
447 impedance, respectively. Equivalent circuit for fitting the spectrum of these phases is
448 shown in **(c)**. CPE denotes constant phase element which has a similar function as
449 capacity but could be used to fit with approximately semicircular-shape spectrum.
450
451 **Fig. 4.** Electrical conductivity of diaspore, δ-AlOOH and ε-FeOOH as a function of
452 reciprocal temperature. Stars, triangles and circles illustrate the conductivity results of

453 diaspore, δ-AlOOH, and ε-FeOOH, respectively.

454

455 **Fig. 5.** Global fitting result of electrical conductivity of diaspore. Solid symbols represent
456 raw conductivity data. Dashed line indicates curves fitted by Eq. (1).

457

458 **Fig. 6.** Trends of the conductivity-depth relation for various lithologies including hydrous
459 minerals in subduction zone at 800K. Dark Blue squares: lawsonite (Pommier et al.,
460 2019); Purple circles: Phengite (Chen et al., 2017); Red triangles: DHMS (Guo &
461 Yoshino, 2013); Orange diamonds: Diaspore (this study); Green circles: ε-FeOOH (this
462 study); Light blue diamonds: δ-AlOOH (this study).

463

464 **Fig. 7.** Comparison between magnetotelluric observations of cold and hot slabs and
465 conductivity-depth profiles of diaspore, δ-AlOOH and ε-FeOOH along the slab surface
466 geotherms. The blue and red solid lines represent the conductivity-depth profiles of the
467 North Philippine Sea (Tada et al., 2014) and the North Cascadia (Meqbel et al., 2014).
468 The blue and red dashed line illustrate the conductivity-depth profiles of diaspore along
469 the slab surface geotherms of the North Philippine Sea and the North Cascadia (Syracuse
470 et al., 2010) within the stability field (Yoshino et al., 2019). The blue dashed-dotted line
471 presents the conductivity-depth profile of ε-FeOOH along the extrapolation of geotherm
472 for the North Philippine Sea. The blue circle represents the results of δ-AlOOH at 20 GPa

and 1200K. The inset shows the stability field of diaspore, δ-AlOOH and ε-FeOOH. The dashed-dotted lines represent the phase diagrams of AlOOH and FeOOH (Yoshino et al., 2019). (1)~(6) represent α-FeOOH, Fe_2O_3+H_2O, ε-FeOOH, diaspore, Al_2O_3+H_2O and δ-AlOOH. The blue and red solid lines represent the slab surface geotherms of the North Philippine Sea and the North Cascadia (Syracuse et al., 2010). Blue dashed line shows extrapolation of the geotherm of the North Philippine Sea, which is used for the calculation of conductivity-depth profile of ε-FeOOH.

Table 1. Experimental conditions and products for sintering and synthesis experiments.

Run No.	P (GPa)	T (K)	Cell size	Starting material	Heater & capsule	Phase
1k2959	8	1100	18/11	Diaspore powder	Graphite MgO	Diaspore
5k3294	19	1273	10/4	Diaspore powder	$LaCrO_3$ MgO	δ-AlOOH
1k2988	8	973	18/11	Diaspore powder	Graphite MgO	Diaspore
1k3181	9	700	18/11	Goethite powder	Graphite MgO	ε-FeOOH
1k3183	9	700	18/11	Goethite powder	Graphite MgO	ε-FeOOH

Table 2. Experimental conditions and products for conductivity measurement experiments.

Run No.	P (GPa)	T (K)	Cell size	Starting material	Heater & capsule	Phase	Grain size (μm)
1k2921	8	500~1000	14/6	Diaspore single crystal	LaCrO3 MgO	diaspore	ND
1k2934	8	500~1100	14/6	Diaspore powder	LaCrO3 MgO	diaspore	ND
1k2950	8, 10, 12, 15	500~1200	14/6	Diaspore powder	LaCrO3 MgO	diaspore	~4
1k2970	8, 10	500~1000	14/6	α-FeOOH powder	LaCrO3 MgO	ε-FeOOH	~2.5
5k3329	20	500~1200	10/3	Pre-synthesized δ-AlOOH	LaCrO3 MgO	δ-AlOOH	ND
5k3333	20	500~1200	10/3	Pre-synthesized δ-AlOOH	LaCrO3 MgO	δ-AlOOH	~2
5k3460	20	500~750	10/3	Pre-synthesized ε-FeOOH	LaCrO3 MgO	ε-FeOOH	ND
5k3461	20	500~800	10/3	Pre-synthesized ε-FeOOH	LaCrO3 MgO	ε-FeOOH	ND
5k3465	20	500~850	10/3	Pre-synthesized ε-FeOOH	LaCrO3 MgO	ε-FeOOH	~11

Note: ND, not determined.

(a)
Diaspore before EC experiments
Diaspore after EC experiments
Diaspore (RRUFF)
Intensity
90
70
50
30
10
-10
20
30
40
50
60
70
80
90
100
2θ (Cu-Kα2)
(b)
δ-AlOOH before EC experiments
δ-AlOOH after EC experiments
δ-AlOOH (Suzuki, 2000)
Intensity
190
140
90
40
-10
25
35
45
55
65
75
85
95
2θ (Cu-Kα2)
(c)
ε-FeOOH before EC experiments
ε-FeOOH after EC experiments
ε-FeOOH (Pernet, 1975)
Intensity
150
130
110
90
70
50
30
10
-10
30
40
50
60
70
80
90
100
2θ (Cu-Kα2)

Figure 1

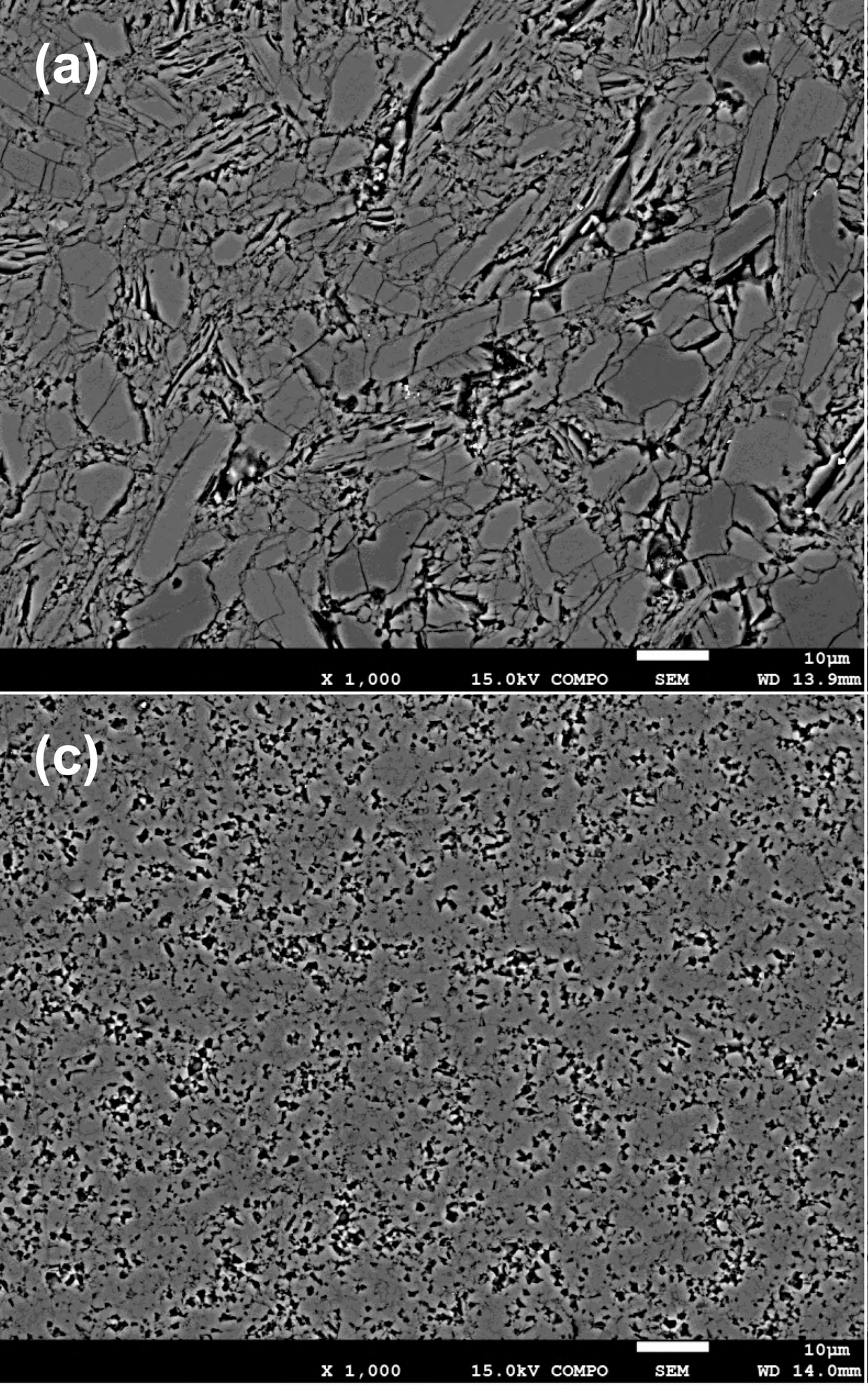
(a)
10µm
X 1,000 15.0kV COMPO SEM WD 13.9mm

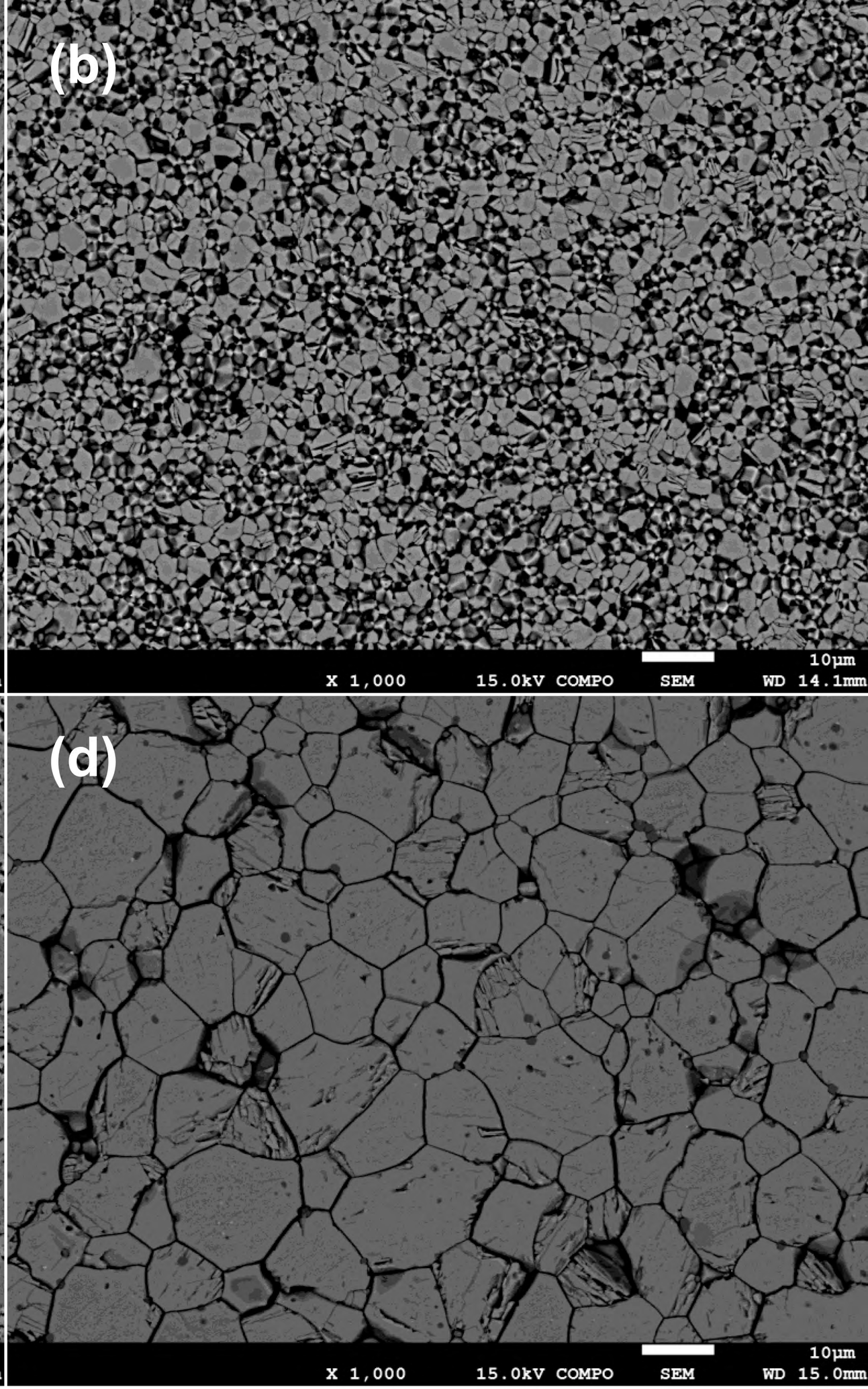
(b)
10µm
X 1,000 15.0kV COMPO SEM WD 14.1mm

(c)
10µm
X 1,000 15.0kV COMPO SEM WD 14.0mm

(d)
10µm
X 1,000 15.0kV COMPO SEM WD 15.0mm

Figure 2

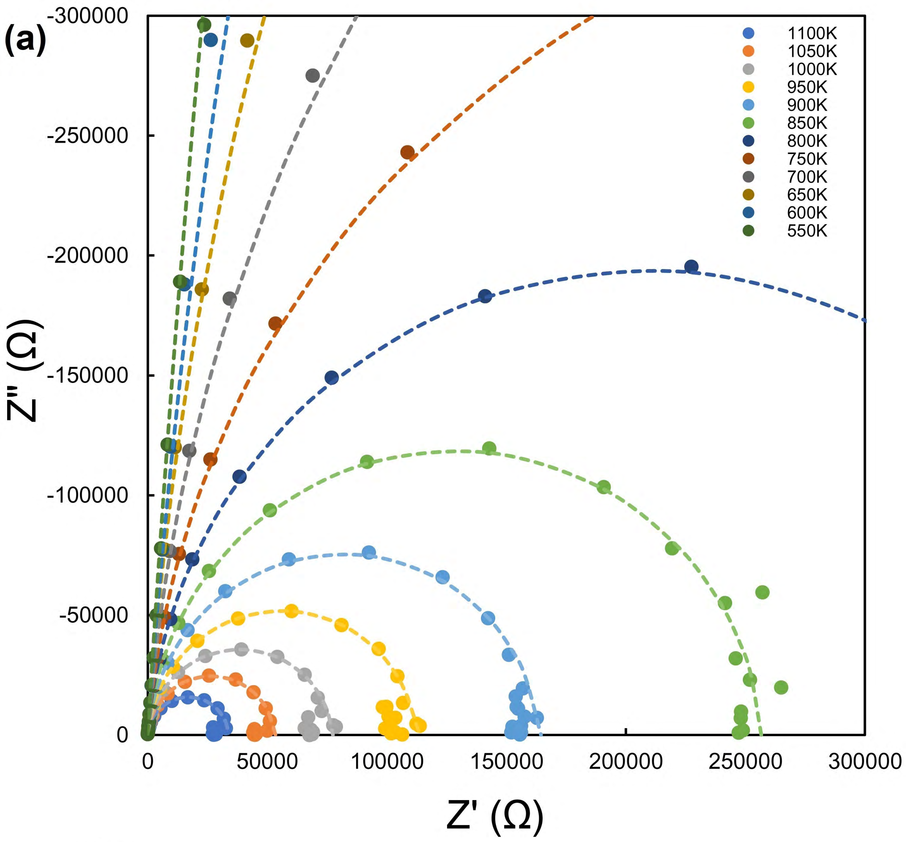
(a)
1100K
1050K
1000K
950K
900K
850K
800K
750K
700K
650K
600K
550K
-300000
-250000
-200000
-150000
-100000
-50000
0
Z'' (Ω)
0
50000
100000
150000
200000
250000
300000
Z' (Ω)

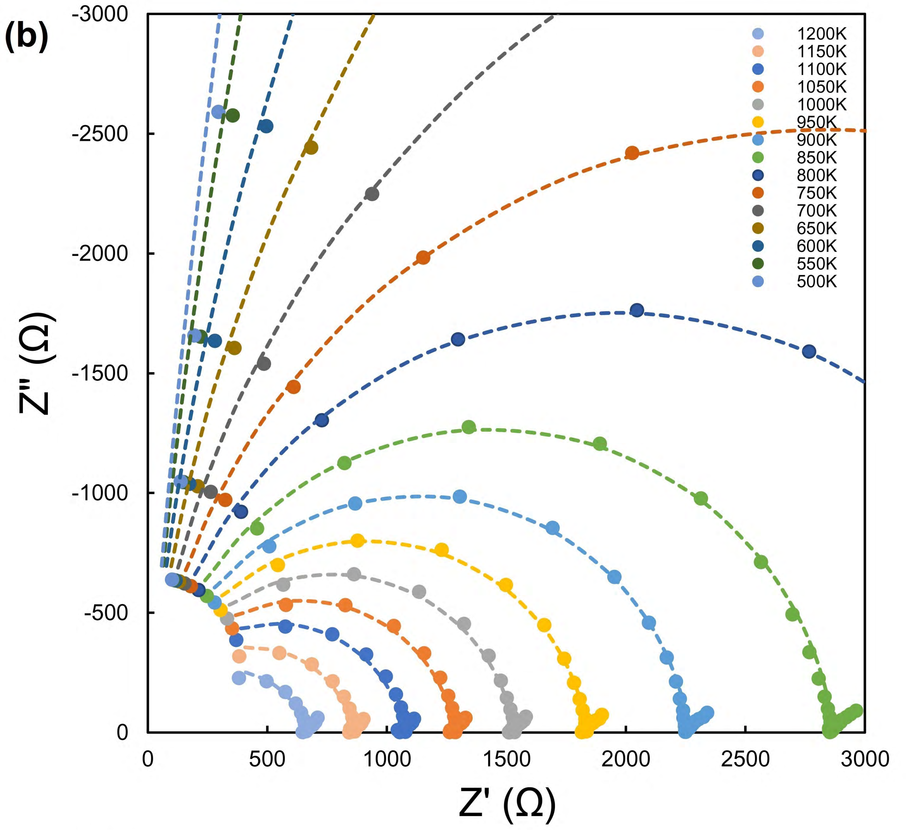
(b)
1200K
1150K
1100K
1050K
1000K
950K
900K
850K
800K
750K
700K
650K
600K
550K
500K
-3000
-2500
-2000
-1500
-1000
-500
0
Z'' (Ω)
0
500
1000
1500
2000
2500
3000
Z' (Ω)

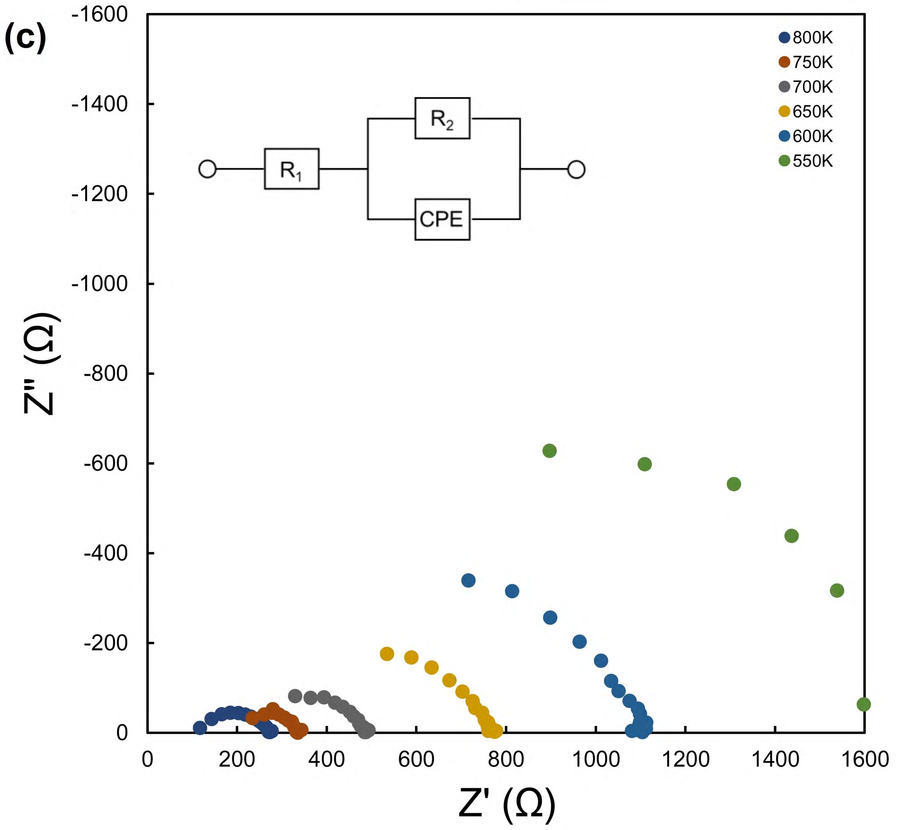
(c)
800K
750K
700K
650K
600K
550K
R1
R2
CPE
-1600
-1400
-1200
-1000
-800
-600
-400
-200
0
Z'' (Ω)
0
200
400
600
800
1000
1200
1400
1600
Z' (Ω)

Figure 3

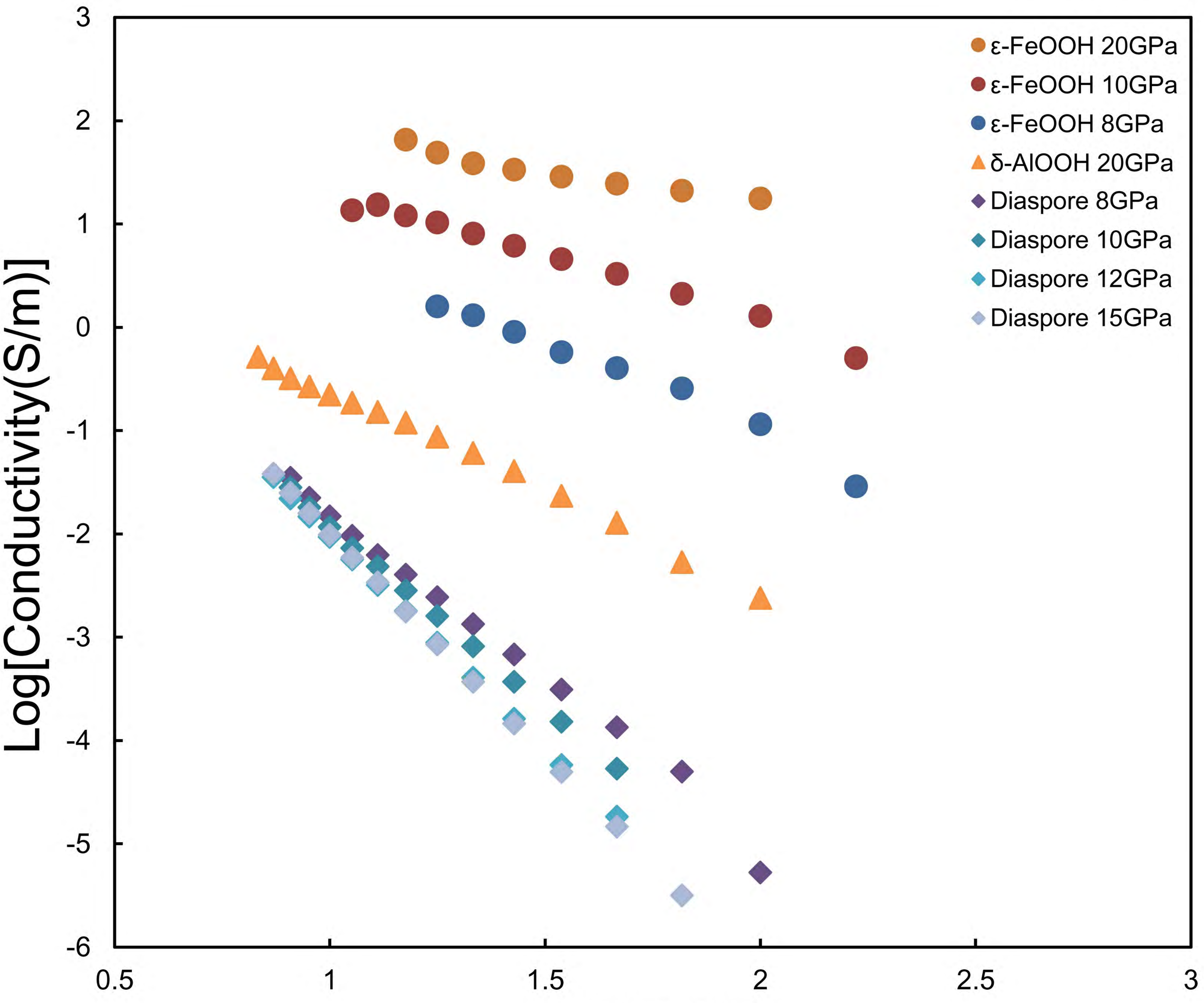
ε-FeOOH 20GPa
ε-FeOOH 10GPa
ε-FeOOH 8GPa
δ-AlOOH 20GPa
Diaspore 8GPa
Diaspore 10GPa
Diaspore 12GPa
Diaspore 15GPa
Log[Conductivity(S/m)]
3
2
1
0
-1
-2
-3
-4
-5
-6
0.5
1
1.5
2
2.5
3
1000/T (K-1)

Figure 4

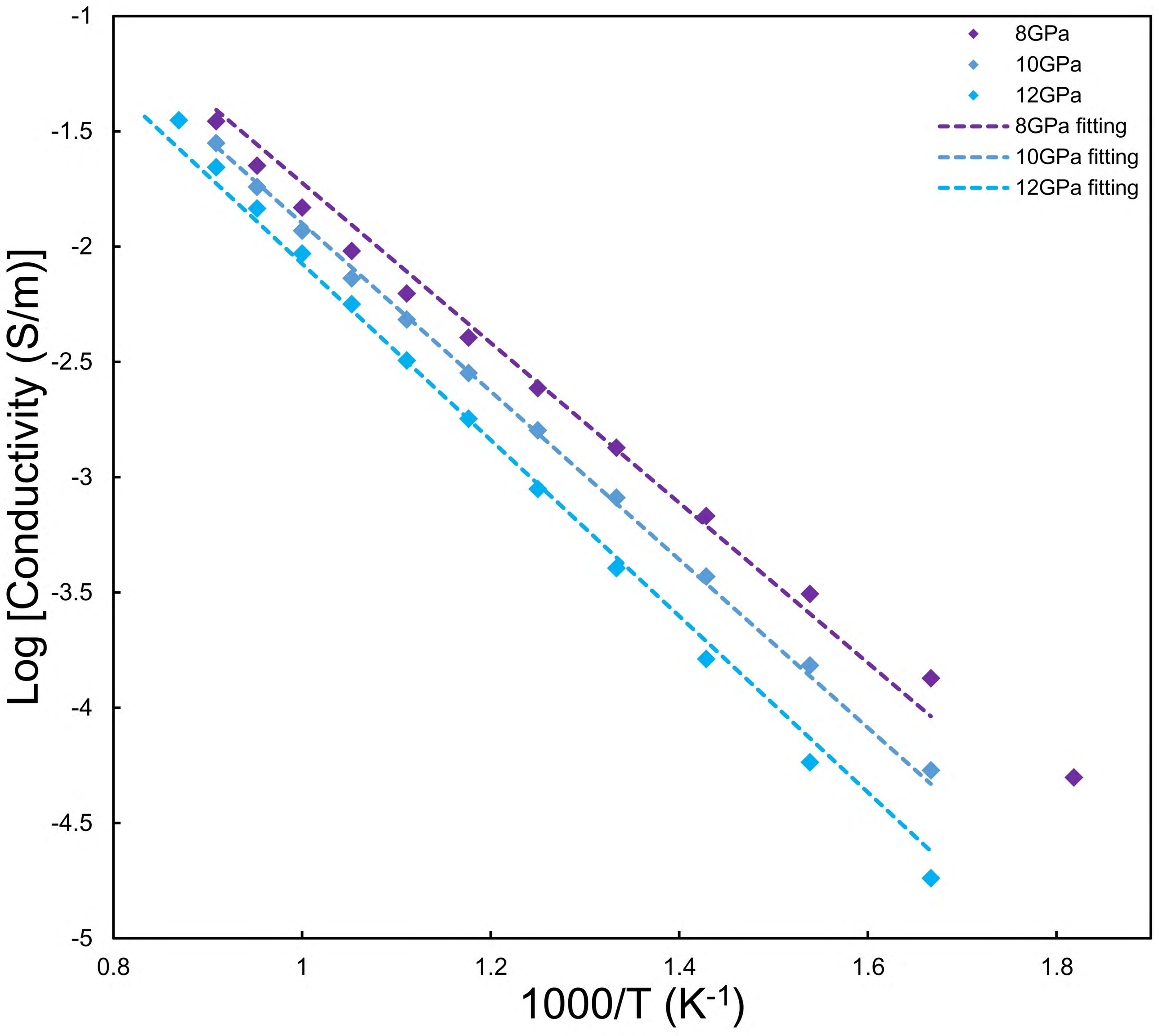
8GPa
10GPa
12GPa
8GPa fitting
10GPa fitting
12GPa fitting
Log [Conductivity (S/m)]
-1
-1.5
-2
-2.5
-3
-3.5
-4
-4.5
-5
0.8
1
1.2
1.4
1.6
1.8
1000/T (K-1)

Figure 5

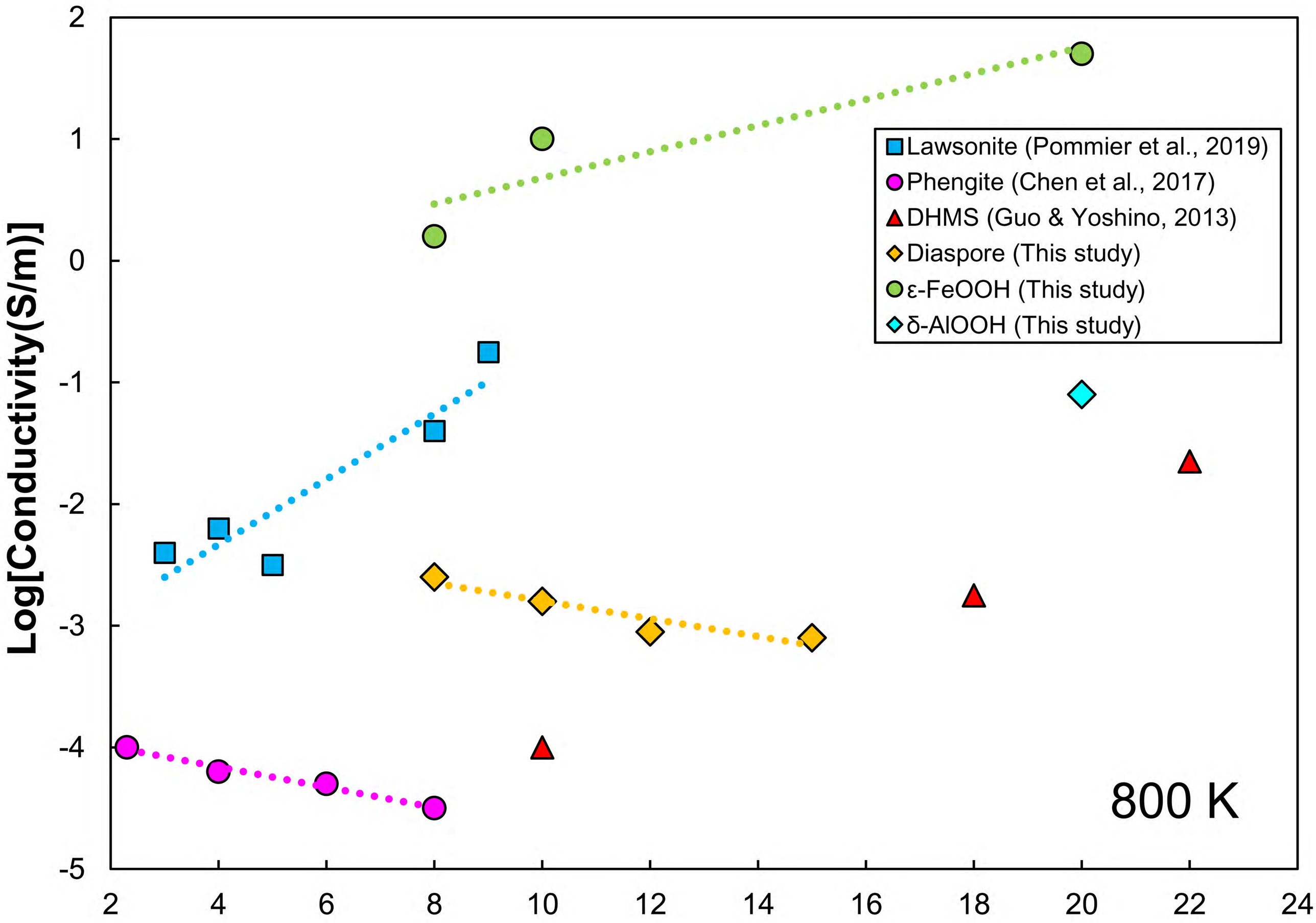
Lawsonite (Pommier et al., 2019)
Phengite (Chen et al., 2017)
DHMS (Guo & Yoshino, 2013)
Diaspore (This study)
ε-FeOOH (This study)
δ-AlOOH (This study)
800 K
Log[Conductivity(S/m)]
Pressure (GPa)
2
1
0
-1
-2
-3
-4
-5
2
4
6
8
10
12
14
16
18
20
22
24

Figure 6

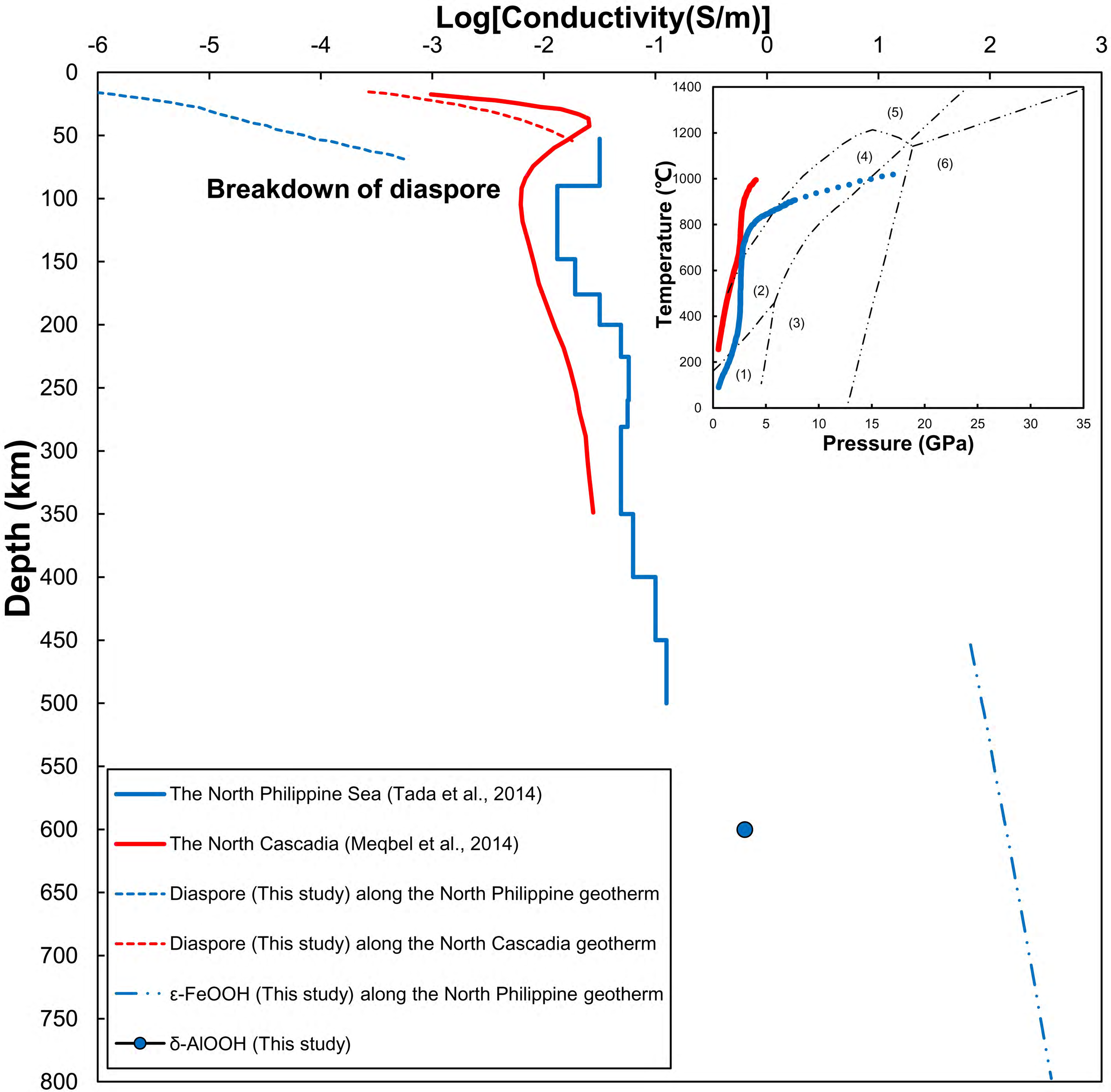
Log[Conductivity(S/m)]
-6
-5
-4
-3
-2
-1
0
1
2
3
Depth (km)
0
50
100
150
200
250
300
350
400
450
500
550
600
650
700
750
800
Breakdown of diaspore
Temperature (°C)
1400
1200
1000
800
600
400
200
0
(1)
(2)
(3)
(4)
(5)
(6)
0
5
10
15
20
25
30
35
Pressure (GPa)
The North Philippine Sea (Tada et al., 2014)
The North Cascadia (Meqbel et al., 2014)
Diaspore (This study) along the North Philippine geotherm
Diaspore (This study) along the North Cascadia geotherm
ε-FeOOH (This study) along the North Philippine geotherm
δ-AlOOH (This study)

Figure 7